Computational Analysis of F-Actin Turnover in Cortical Actin Meshworks Using Fluorescent Speckle Microscopy

A. Ponti,* P. Vallotton,* W. C. Salmon,† C. M. Waterman-Storer,† and G. Danuser*
*BioMicroMetrics Group, Laboratory for Biomechanics, ETH Zurich, 8952 Schlieren, Switzerland; and †Department of Cell Biology and Institute for Childhood and Neglected Diseases, The Scripps Research Institute, La Jolla, California 92037 USA

ABSTRACT Fluorescent speckle microscopy (FSM) is a new imaging technique with the potential for simultaneous visualization of translocation and dynamic turnover of polymer structures. However, the use of FSM has been limited by the lack of specialized software for analysis of the positional and photometric fluctuations of hundreds of thousand speckles in an FSM time-lapse series, and for translating this data into biologically relevant information. In this paper we present a first version of a software for automated analysis of FSM movies. We focus on mapping the assembly and disassembly kinetics of a polymer meshwork. As a model system we have employed cortical F-actin meshworks in live newt lung epithelial cells. We lay out the algorithm in detail and present results of our analysis. The high spatial and temporal resolution of our maps reveals a kinetic cycling of F-actin, where phases of polymerization alternate with depolymerization in a spatially coordinated fashion. The cycle rates change when treating cells with a low dose of the drug latrunculin A. This shows the potential of this technique for future quantitative screening of drugs affecting the actin cytoskeleton. Various control experiments demonstrate that the algorithm is robust with respect to intensity variations due to noise and photobleaching and that effects of focus plane drifts can be eliminated by manual refocusing during image acquisition.

INTRODUCTION

Fluorescent speckle microscopy (FSM) is a recently developed method to analyze the movement, assembly, and disassembly dynamics of macromolecular structures in vivo and in vitro (Waterman-Storer and Danuser, 2002). Originally, it has been applied to the analysis of in vivo microtubule movements in mitotic spindles and actin retrograde flow in migrating cells (Waterman-Storer et al., 1998), and has now become the tool of choice for investigating many aspects of cytoskeleton dynamics. Speckled images of such polymer structures are obtained by microinjecting low amounts of labeled monomers into cells. Random incorporation of few labeled and many endogenous unlabeled monomers into cellular structures yields a fluorophore distribution with high spatial density variation, which is, by light microscopic imaging, convolved with a diffraction-limited point spread function. We define a speckle as a peak in the image signal, significantly brighter than its surroundings. Most of the speckle data hitherto published refer to multifluorophore speckles formed by 3–7 fluorophores clustered within a diffraction-limited region, and only recently Watanabe and Mitchison (2002) were able to acquire single-fluorophore speckles in actin structures in fibroblasts.

Speckles act as local reporters throughout the polymer lattice. In time-lapse FSM, speckle appearance and disappearance are linked to polymerization and depolymerization, whereas speckle movement is associated with polymer translocations. Therefore, FSM allows simultaneous and local measurements of polymer turnover and movement in large areas of the cell, with a time resolution equal to the frame rate of the movie. This offers a novel tool for studying nonsteady-state molecular processes in live cells.

In this paper we apply FSM to the study of cortical F-actin meshwork dynamics in contact-inhibited newt lung epithelial cells. Contact-inhibited cells form tight adherens junctions with neighboring cells (Harris, 1999). In contrast to migrating cells, where F-actin meshworks and thus actin fluorescent speckles undergo a coordinated motion known as ''retrograde flow'' (Abercrombie et al., 1972; Small, 1981; Wang, 1985; Forscher and Smith, 1988; Danuser and Oldenbourg, 2000; Salmon et al., 2002), in contacted cells cortical F-actin meshworks remain spatially stationary. However, FSM movies still show a strong photometric activity, indicating that F-actin is undergoing steady turnover (Waterman-Storer et al., 2000). We investigated how to extract quantitative information of this turnover to shed new light on the mechanisms of actin dynamics. Our long-term goal is to develop a quantitative live-cell assay to study the effect of biochemical reagents, molecular, and genetic factors involved in the regulation of actin dynamic processes.

Speckles are a weak and inherently stochastic image feature with a low signal-to-noise ratio (SNR). For this reason, any measurement derived from FSM data must rely on a statistical processing of large numbers of speckles. Typically, FSM movies contain >500,000 speckles that fluctuate in intensity, move and disappear, while new speckles appear. Speckle fluctuations are induced by stochastic molecular processes and their interpretation requires mathematical models of the relation between changes in speckle signal and the alteration of the polymer. Hence the demand for computational tools, where each speckle is automatically tracked in position and intensity and statistically processed according to the models.

Submitted August 19, 2002, and accepted for publication December 9, 2002.

Address reprint requests to G. Danuser, Tel.: +41-1-633-6214; Fax: +41-1-633-1124; E-mail: danuser@biomech.mavt.ethz.ch.

0006-3495/03/05/3336/17 $2.00

In the core of this paper we propose a first version of an algorithm working along these lines and we demonstrate its performance on synthetic and experimental data. Materials and Methods introduces the experimental protocols and a simulation package that enabled us to establish a forward model of speckle formation dependent on several biochemical and imaging parameters. Artifacts in the imaging and analysis steps are discussed in the concluding section along with a summary of the key features of our computational model.

MATERIALS AND METHODS

Software development

All programs for speckle analysis and graphical representation have been written in house using MATLAB version 6.0 (The MathWorks, Natick, MA). The computation is performed on high-end PCs running either Windows or Linux operating systems.

Synthesis of FSM movies using Monte Carlo simulations of dynamic F-actin meshworks

For code debugging and to investigate the relationship between speckle lifetime and polymer turnover in a complex macromolecular structure, we implemented a Monte Carlo simulation of how fluorescently labeled and unlabeled monomers dynamically associate and dissociate from an F-actin meshwork. The physical model is depicted in Fig. 1 *a*. In such a meshwork, the 3D distribution of fluorophore is determined by a contribution of three random processes: i), distribution of free barbed and pointed ends of actin filaments; ii), rates of association and dissociation of actin monomer at the two filament ends (Pollard, 1986); and iii), binomial sequence of labeled and unlabeled monomers turned over at all free ends. Image data was synthesized by convolution of the simulated fluorophore distribution with a 3D model point spread function of the microscope plus by random addition of Poisson-distributed shot noise, and normal distributed camera dark and readout noise. The program simulates the distribution of barbed and pointed ends based on a user-specified function defining the spatial variation in area concentrations of the two kinds of ends. This allowed us to simulate F-actin meshworks with spatially modulated probabilities of assembly and disassembly. Once the barbed and pointed end distributions and the concentration of monomer are set, the meshwork locally assembles and disassembles. If necessary, a steady state, i.e., monomers associate to and dissociate from the meshwork at on average equal rates, can be simulated by periodic redistribution of the free ends. In this implementation, the model was useful to validate our software for kinetic analysis (see Results) but it cannot reveal any relationship between the observable speckle intensity fluctuations and regulatory factors of F-actin turnover. In particular, the simulation does not include chemical reaction equations other than the stochastic rate equations of monomer association and dissociation. A more complex modeling of these rates as functions of a network of interdependent chemical equilibriums affected by numerous effectors upstream of F-actin turnover is a challenging future task. It is now addressable in combination with our new quantitative FSM experiments that can test the roles of specific effectors under drug perturbation.

Despite the many oversimplifications, the model was sufficiently accurate to produce speckled images (Fig. 1 *a*) and to teach us a critical lesson about FSM of a polymeric meshwork: the speckle number density is almost independent of whether the meshwork assembles or disassembles; but depends only on the point spread function (PSF) volume. With $NA = 1.4$ optics, the number density is 3.5–4 speckles per μm^2 (Fig. 1 *b*). The graph in Fig. 1 *b* displays the mean speckle number density from five simulations of a meshwork that assembles for 120 s and disassembles for 360 s at equal rates (*inset*: mean fluorescence intensity development). The steady-state speckle number density is reached after 100 s. The fact that the speckle density remains constant despite further addition of labeled monomer suggests that monomer association can cause an equal number of speckle appearances (births) as disappearances (deaths). The same holds for dissociation. This finding caused us to develop the classification scheme of speckle birth and death, which is now the core of the algorithm for kinetic analysis (see Algorithm). Data such as presented in Fig. 1 were used to prove the concepts of the algorithm and to verify their performance (see Results).

Cell manipulations

Primary cultures of newt lung epithelial cells were established on 22 × 22 mm No. 1.5 coverslips from *Taricha granulosa* lung tissue and maintained in Rose Chambers at ~20°C in half strength L-15 media containing 5% FBS, antibiotics, and antimycotics as previously described (Waterman-Storer and Salmon, 1997; Reider and Hard, 1990). We microinjected 0.5 mg/ml X-rhodamine labeled actin (prepared as described in Waterman-Storer, 2002) into newt lung epithelial cells that were contacted on all sides by neighboring cells and situated in the center of the epithelial sheet that extends from the explant of lung tissue during the wound healing response in culture. For FSM imaging, coverslips of injected cells were mounted on slides on two strips of double-stick tape in culture media containing 30 U/ml of Oxyrase (to inhibit photobleaching) (Oxyrase, Mansfield, OH) and sealed with valap (1:1:1 mixture of Vaseline, lanolin, and paraffin). For some experiments, injected cells were fixed in 4% paraformaldehyde in PBS (140 mM NaCl, 15 mM Na-phosphate, 2.5 mM KCl, 1.6 mM K-phosphate, pH 7.2) for 5 min, rinsed in PBS, and mounted on slide/tape chambers in cell culture media with or without Oxyrase. For latrunculin-A perfusion experiments, coverslips of cells were mounted in a custom-built perfusion

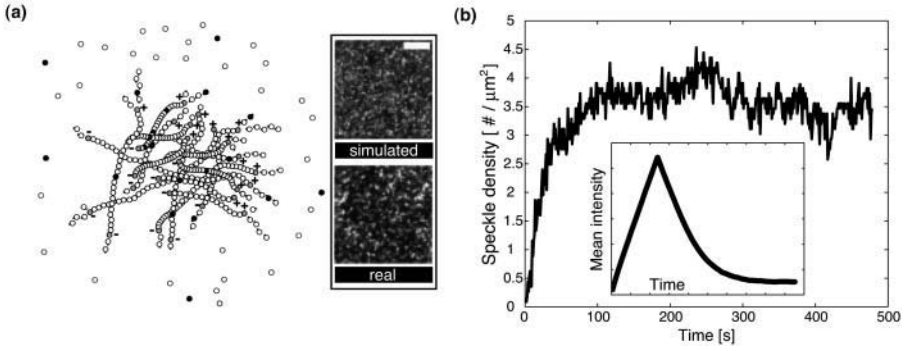

FIGURE 1 Dynamic simulations of a polymerizing and depolymerizing F-actin meshwork. (*a*) Physical model for the generation of an actin meshwork. The inset shows a comparison between simulated and real FSM image data. Scale bar, 1 μm. (*b*) Mean speckle number density from five simulations of a meshwork that assembles for 120 s and disassembles for 360 s at equal rates (*inset*, mean fluorescence intensity development). Meshwork disassembly is associated with a decrease in the mean intensity. Once the steady-state speckle number density is reached (after 100 s), the mean speckle density is independent of whether the meshwork is polymerizing or depolymerizing, but only dependent on the PSF volume. With $NA = 1.4$ optics, the number density is 3.5–4 speckles per μm^2.

chamber that was sealed to ambient air in media containing Oxyrase, and gravity-perfused with media containing 750 nM latrunculin A and Oxyrase.

Time-lapse spinning disk confocal FSM

Time-lapse FSM was performed using a spinning disk confocal microscope system on an inverted microscope (TE300 Quantum, Nikon, Melville, NY) using a 100× 1.4NA Plan-Apochromatic DIC objective lens. Light from a 50 mW Krypton-Argon ion laser (OmniChrome/Melles Griot, Irvine, CA) was delivered by a single-mode fiber optic (Point Source) to the UltraView spinning disk confocal scan-head (PerkinElmer, Wellesley, MA). Excitation wavelength was selected by a filterwheel apparatus (Lamda10-2, Sutter Instruments, Novato, CA) containing excitation filter for 568 nm (Chroma, Brattleboro, VT) and an opaque disk for use as an excitation shutter. Images with an average exposure time of 1.5–2 s were collected at 5-s intervals on an Orca 2 camera (Hamamatsu, Bridgewater, NJ) containing a 1280 × 1024 array of 6.7 × 6.7 μm pixels in progressive scan interline transfer configuration operated in the slow-scan (1.25 mHz) 14 bit-depth mode, where the noise is typically 3–5 electrons rms. Focus was controlled by a stepper motor (Ludl Electronic Products, Hawthorne, NY). Microscope functions were controlled by MetaMorph (Downingtown, PA) software on a PC computer.

Characterization of image noise

Titration experiments

Solutions of varying concentrations of X-rhodamine-labeled actin (0, 8, 15, and 22 μM) were prepared in G-buffer (2 mM Tris, 0.2 mM $CaCl_2$, 0.2 mM Mg ATP, 0.5 mM β-mercaptoethanol, pH 7.0); 0.8 μl of solution was squashed between a slide and a 22 × 22 mm coverslip, and the coverslip sealed to the slide with valap. This reproducibly gives a layer of solution that is ~4 μm thick. Images of the solution just adjacent to the coverslip surface were then acquired with the spinning disk confocal system for each concentration with exposure times in an interval ranging from 500 ms to 3000 ms in 100 ms steps.

Calibration of a noise model

For the estimation of noise parameters at different exposure times, a calibration of the camera was performed. For four concentrations of X-rhodamine-actin solutions (0 μM defining the dark field, 8, 15, 22 μM), 11 images were acquired per exposure time setting (see Titration experiments). From the dark-field image series, the parameters I_0 and α_{DN} in Eq. 2 (see Algorithm—Statistical selection of speckles) were estimated. The mean of all pixel intensities over 11 images defined the value for I_0. To estimate α_{DN}, the intensities $I(x,y)$ of the 11 dark-field images were first analyzed in a position-dependent fashion, providing variances $\sigma^2_{DN}(x,y)$. The average of this variance field provided a measure for the dark and readout noise α_{DN}.

Variances σ_i^2 were calculated for all other concentrations $i = 8, 15, 22$ μM in the same way, and the mean intensity I_i was used to define the intensity dependence of noise according to $\sigma_i^2 - \alpha_{DN} = \beta(I_i - I_0)$ (see Eq. 2). The parameter β was estimated by linear regression of the data pairs (σ_i^2, I_i).

ALGORITHM

We describe an algorithm for the extraction of kinetic parameters of F-actin turnover from time-lapse FSM in otherwise stationary meshworks, as they occur in contact-inhibited cells. A typical FSM movie consists of 100–200 frames at sampling rates between 1 and 5 s per frame. A graphical outline of the algorithm is given in Fig. 2.

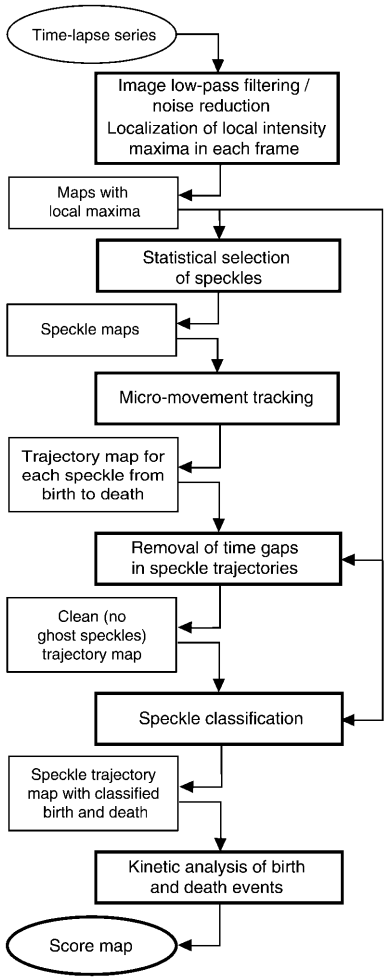

FIGURE 2 A computational scheme for kinetic analysis of FSM data (see text for details).

Noise reduction and local maximum selection

The F-actin cytoskeleton acquires its speckle pattern due to random incorporation of actin monomers into actin filaments at a very low labeling ratio (<0.5%). The labeling ratio f is defined as the fraction of labeled monomers in the entire cytoplasmic monomer pool. This results in a high spatial variation of the fluorophore density, which, after imaging with high magnification diffraction limited optics, appears as a band-limited signal with a random texture of intensity maxima and minima. We define a speckle as a local intensity maximum in the fluorescence signal, associated with a locally high density of fluorophores. In multifluorophore FSM, a speckle corresponds to a clustering of 3–7 fluorophores in an area defined by the lateral extension of the microscope PSF (Waterman-Storer and Salmon, 1999). A speckle can thus be regarded as a local probe in the actin meshwork, in which fluctuations in the signal intensity indicates polymer turnover with high temporal and spatial localization. The maximal spatial resolution achievable is defined by the mean

distance between two distinguishable speckles; the temporal resolution is defined by the frame rate of the movie.

In the raw FSM image data, many of the observed local maxima are, however, not due to locally clustered fluorophores, but due to noise. To separate noise from speckles, we rely on the fact that pixel intensities belonging to one speckle are spatially correlated over the radius of the PSF, whereas intensity variations due to noise are independent between pixels. Convolving the signal with a low-pass filter with a frequency cutoff ν_c equal to the bandpass of the optical transfer function will guarantee preservation of the speckle signal while suppressing noise at spatial frequencies higher than ν_c. For numeric stability we apply a Gaussian kernel for low-pass filtering

$$G(r,s) = \frac{1}{\sqrt{2\pi s^2}} \cdot e^{-1/2(r^2/s^2)}, \quad (1)$$

instead of a kernel with a sharp cutoff ν_c. The parameter $r^2 = x^2 + y^2$ in Eq.1 denotes the distance of a pixel contributing to the convolution from the center of the Gaussian kernel, and the parameter s defines the filter drop off. We determined the latter in agreement with the PSF of our spinning disk confocal microscope. Under conditions identical to our FSM experiments, Maddox et al. (2003) measured a PSF full width at half-maximum (FWHM) of 260 nm using subresolution fluorescent beads. Expressed in the image domain, this results in an FWHM of 3.9 pixels. Therefore, we set the parameter s of the Gaussian kernel to 1.25 pixels to match the experimental FWHM and the FWHM of our noise filter.

After low-pass filtering, we apply a local maximum detection in a 5×5 pixel mask:

$$L = \{L_i\},\ \forall i\{I(\mathbf{x}_i) > I(\mathbf{x}_i + \mathbf{t}) \text{ with } \mathbf{t} = [t_1, t_2]; t_1, t_2 = -2, \ldots, 2\}.$$

The size of the mask is again motivated by the diameter of the PSF. Each local maximum is a speckle candidate. Typically, several thousands of them are extracted by this first algorithmic step.

Statistical selection of speckles

With the choice of a noise filter with the same FWHM as the PSF and thus an almost identical frequency cutoff as the optical transfer function, noise components corresponding to spatial frequencies below the optical cutoff are still present and interfere with the proper speckle signal. Therefore, many of the local maxima are still due to noise and are not associated with an actual speckle. The set L has to be divided into two subsets $L = S \cup L_N$, where the set S contains local maxima representing speckles and L_N contains weak local maxima due to noise.

The set partitioning relies on a noise model permitting a test of each local maximum for its statistical significance. We assume that the image noise is a superposition of two independent components, dark noise and shot noise (Oshiro, 1998). The dark-noise component can be modeled as an additive and normal distributed random variable with a variance σ^2_{DN}. Shot noise is proportional to the signal intensity and needs to be calibrated once for every experimentally applied exposure time. It is Poisson distributed with the mean number of photons representing the mode of the distribution and a variance σ^2_{SN} proportional to the number of photons (Papoulis, 1991). In total, we describe noise as the variance of the intensity I

$$\sigma^2 = \sigma^2_{DN} + \sigma^2_{SN},$$

with

$$\sigma_{SN} = \gamma(I - I_0)^{1/2}.$$

The parameter I_0 is the camera offset expressed in gray levels. The coefficient γ defines the proportionality factor between the square root of the offset-corrected image intensity and the variance of the image signal induced by shot noise. Consequently, the total variance can be written as a linear function of intensity:

$$\sigma^2(I) = \alpha + \beta(I - I_0), \quad (2)$$

with $\alpha = \sigma^2_{DN}$, and $\beta = \gamma^2$. The parameter β has been calibrated once for our imaging system (see Materials and Methods). It remains constant between experiments, unless there is a change in the applied camera gain or exposure time. In contrast, the camera offset and dark noise slightly vary between image stacks. Therefore, the values for α and I_0 are recalculated for every time-lapse series by analyzing background regions without fluorescent signal. Expressed in the normalized intensity range [0, 1] used for all image data processing, the value for β determined amounted to 2.00×10^{-4}, and the value for the dark noise σ_{DN} averaged over several movies was 2.73×10^{-4} with $\bar{I}_0 = 2.84 \times 10^{-2}$. Converted into the intensity range of our 14-bit CCD camera this corresponds to a camera offset of 472 gray levels with a dark noise of five gray levels. Speckle peak intensities reached 630 gray levels at maximum. Applying Eq. 2 to this signal yields a combined dark and intensity-dependent noise of 18 gray levels. This example also illustrates the maximum SNR found in our FSM data. Defining the SNR of a speckle as the ratio between peak intensity above background and the noise level propagated for this intensity difference, we obtained signals with $SNR_{max} = 8.5$ at best.

Using the noise model, an intensity-dependent confidence interval ΔI_C can be calculated for each local maximum in L. Maxima with a peak intensity (I_L) that is in a statistical sense more than ΔI_C above the adjacent background (I_{BG}) are accepted as speckles and thus added to the set S. Maxima not satisfying this criterion are assigned to the set L_N. Fig. 3 illustrates this notion of a speckle as a statistically significant

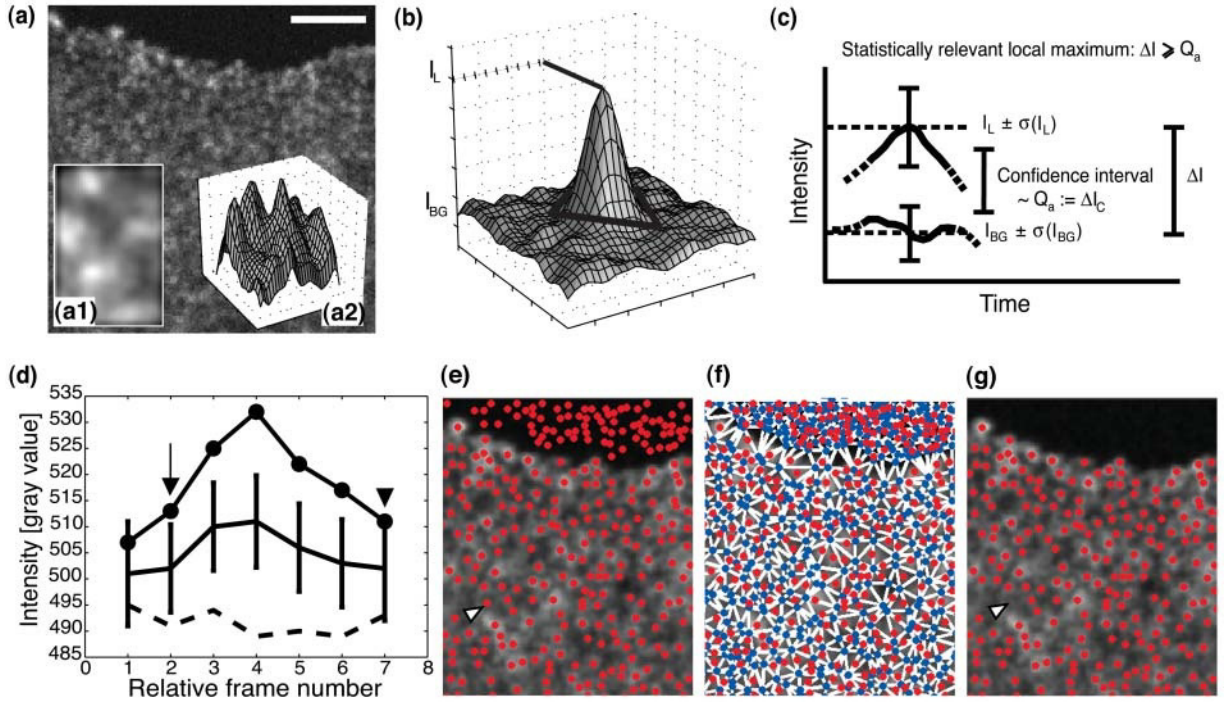

FIGURE 3 Separation of speckles, i.e., significant local maxima in the image from noise-related weak local maxima. (*a*) Images are low-pass filtered to remove high-frequency noise. Scale bar, 2.5 μm. (*Inset a 1*) Zoom-up of a subregion after filtering. (*Inset a 2*) The same subregion displayed as an intensity function in $\mathbb{R}^2$. (*b*) Definition of a speckle as an intensity peak above background. (*c*) Principles of statistical speckle selection (see text for additional explanations). (*d*) Example of a speckle lifetime history; time point of speckle birth (*arrow*) and time point after speckle death (*arrowhead*). (*e–g*) Statistical selection of speckles illustrated on an image. (*e*) Result of local maximum (*red dots*) extraction. (*f*) Local minima (*blue dots*) extraction and assignment of background intensities to local maxima by Delaunay triangulation of local minima (see text). (*g*) Local maxima failing the Student's *t*-test are not counted as speckles. The arrowheads in *e* and *g* indicate the position of one weak local maximum falling through the statistical selection.

image feature. Fig. 3 *a* displays the speckled fluorescence intensity image of F-actin in a living cell, of which Inset *a 1* shows a zoom-up window represented in *a 2* as a continuous function in $\mathbb{R}^2$. Fig. 3 *b* shows an isolated speckle with peak intensity I_L above a relatively homogeneous background intensity I_{BG}. Notice that the background intensity is not always as clearly defined as in this case but that generally it has to be extracted from intensity distributions with rather complicated topographies (see *a 2*). A procedure for the calculation of the background is discussed later in this section. Given the peak and background intensities, the difference ΔI between the two has to exceed the critical interval ΔI_C to render a local maximum a speckle. This is depicted by Fig. 3 *c*, where the two levels differ more than the required confidence interval. As it will be introduced in Eq. 4, the size of the interval is a function of the estimated noise in the two intensity values. Fig. 3 *d* already suggests a possible development of a speckle throughout its lifetime of, in this case, five frames. It starts out as a nonsignificant local maximum (*frame 1*) before it turns into a speckle (*arrow* in *frame 2* indicates the speckle birth). To illustrate the statistical conditions, the critical interval ΔI_C is plotted at the midpoint between the peak and background intensities. As long as the speckle is alive (*frames 2–6*), the peak-to-background intensity difference is greater than the critical interval, whereas the speckle turns again into an insignificant local maximum at frame 7 (*arrowhead*). Speckle death occurs at the last time point where the peak intensity I_L is significantly higher than the background intensity I_{BG} (*frame 6*).

Obviously, the entire selection procedure depicted by Fig. 3, *a–d*, relies on an estimate of the local background for each element in L. In analogy to the procedure for local maximum detection, local minima are sought in every image. Fig. 3, *e–g*, displays the different steps of speckle selection. Fig. 3 *e* shows a portion of the low-pass filtered image of speckled actin in a living cell overlaid with local maxima (*red dots*). In Fig. 3 *f*, the local minima (*blue dots*) are displayed. Using Delaunay triangulation, these points are connected to form a meshwork (*white solid lines*). By definition, Delaunay triangles have the property that the circumscribing circle of each triangle does not contain vertices from any other triangle in the meshwork. Therefore, every local maximum can be unambiguously assigned to a triangle of three local minima (Fig. 3 *f*), of which the mean intensity $\bar{I}$ provides a measure I_{BG} for the background intensity. Using Eq. 2, uncertainties for both the local maximum intensity $\sigma(I_L)$, and the background intensity $\sigma(I_{BG})$, can be derived (cf. Fig.

3 *c*). In mathematical terms, the statistical test for speckle selection then amounts to performing a Student's *t*-test with a user-defined confidence probability α:

$$H_0 : |\Delta I| = 0; \quad \text{with } \Delta I = I_L - I_{BG};$$
$$H_A : |\Delta I| > 0;$$
$$T = \frac{|\Delta I|}{\sigma_{\Delta I}} \propto t_\infty(0,1); \tag{3}$$

with

$$\sigma^2_{\Delta I} = \sigma^2(I_L) + \frac{1}{3}\sigma^2(I_{BG}). \tag{4}$$

H_0 is rejected if $T \geq Q_\alpha$, where Q_α is the Student's *t*-quantile. Notice in Eq. 4 that the contribution of the background to the variance of the intensity difference is three times smaller than the one of the local maximum. This is because the background value is an estimate based on three intensity values.

The result of the statistical test is displayed in Fig. 3 *g*. The selection step removes a few weak local maxima from the background, although in the example shown most of the local maxima are retained as significant. This suggests that many noise-induced image features are already removed in the initial low-pass filtering. The arrowheads in Fig. 3, *e* and *g*, indicate the position of one weak local maximum not suppressed by low-pass filtering and failing to pass the statistical test. This almost ideal scenario, however, deteriorates with image artifacts that cause sudden fluctuations and fading of the speckle contrast associated, for example, with in- and out-of-focus movement of the sample. In such situations substantially more weak local maxima are eliminated.

Micromovement tracking

After selection of speckles, their microscopic movements are tracked over time. A speckle at time point t is linked to a speckle at time point $t + 1$, if the distance between the two positions is less than or equal to half the diameter of the Airy disk. This is motivated by the fact that the mean distance between two speckles in the same frame is generally higher. Exceptions to this rule occur with overlapping speckles, although most of these overlaps are eliminated by the low-pass filtering. The few remaining cases are currently neglected by our software. The position of each speckle varies over time even in spatially stationary actin meshworks as studied in this work. This is due to physical effects, such as Brownian motion and motor protein-induced meshwork contractions, as well as signal effects caused by the addition or removal of fluorescent label near an existing speckle. Also the presence of a noise-induced local maximum nearby a speckle will significantly shift the speckle position during low-pass filtering. In this context, it must be noticed that the signal contribution due to free actin monomers diffusing through the cytosol does not affect either the position or the intensity of a speckle. Given a diffusion rate of 47 pixels/s in our imaging system (Abraham et al., 1999), the signal generated by a labeled but unbound monomer in one pixel is, over the exposure time of 0.5–3 s used in FSM, one to two orders of magnitude smaller than the one of a bound monomer. This was recently demonstrated by Watanabe and Mitchison (2002), where even the more critical case of single fluorophore speckles was examined.

If a speckle at time t cannot be linked to a speckle at time $t + 1$ according to the above criterion, it is classified as a dying speckle. On the contrary, speckles in $t + 1$ that are not linked to speckles in t are classified as new speckles. As a result, the micromovement tracker provides speckle trajectories existing between frames t_b (time of birth) and t_d (time of death). Sometimes, newly born speckles cannot be linked to any other speckle in the following frame. In this case, t_b equals t_d. They are referred to as ghost speckles. The existence of ghost speckles is expected from a statistical point of view, because speckles are indeed weak features with a low signal-to-noise ratio. However, they also occur with failures in the tracking or with the fusion and dissolution of multiple speckles. Both situations are not yet optimally addressed by our software, and we suppose that a certain percentage of ghost speckles are not associated with short-living features but with suboptimal analysis (see also Discussion).

After the identification of trajectories, the software stores for each speckle peak and background intensities, speckle position, and the positions of the three local minima at every time point t ($t_b \leq t \leq t_d$). Furthermore, the same information is stored for the last time point $t_b - 1$ before birth and for the first time point $t_d + 1$ after death. The importance of this additional information will be discussed below.

The speckle trajectories may be interrupted sometimes because of peak and background intensity fluctuations that yield failures of the test in Eq. 3. Consequently, speckle lifetimes are underestimated and many artifactual birth and death events will be accumulated. This problem must be addressed before kinetic analysis of birth and death events.

Removal of time gaps in speckle trajectories

To circumvent the problem of false speckle birth and death detection, all birth and death events are analyzed individually. If a speckle that disappears at time $t - 1$ is spatially close (not farther than the Airy disk radius) to a speckle that appears at time $t + 1$, meaning that at time t there is no significant local maximum that links the two fragments, the gap in t can be closed if and only if there exists a weak local maximum in $L_N(t)$ with a position in the same neighborhood. If this is the case, the maximum in $L_N(t)$ is moved to the set $S(t)$. The gap is closed, and two apparent events (one death and one birth) are removed from the event list. Fig. 4 illustrates the intensity development of a speckle with five closed gaps (*arrows*). The dashed line indicates the critical intensity difference. Small fluctuations in the peak and background intensities cause an

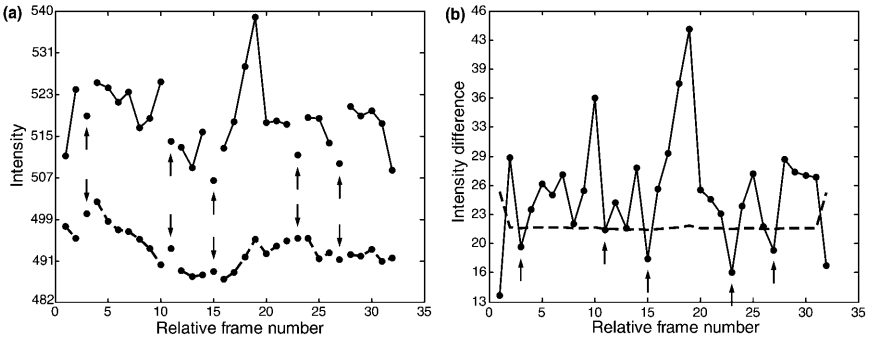

FIGURE 4 Gap closer. (*a*) The linking of six short-living speckles (*full lines*) separated in time by one frame and in space by less than the Airy disk diameter removes false birth and death events and reconstructs one long-living speckle (*b*). The linking of two speckles is only allowed if the gap frame contains a weak local maximum within distance of the Airy disk radius to both the false death position of the first speckle and the false birth position of the second speckle (*arrows* in panel *a*). Further details on the linking conditions are given in the text. Panel *b* displays the intensity differences $\Delta I = I_L - I_{BG}$ between peak and background, superimposed by the critical intensity difference ΔI_C calculated with the noise model (*dashed line*).

initial fragmentation of one speckle into several subspeckles, which are fused by the gap closer.

The importance of suppressing false birth and death events will become evident as we describe the algorithm further. For the remainder of the article, we will refer to the complete speckle trajectory, including the development of peak and background intensities, simply as a speckle.

Classification of birth and death events

Waterman and Salmon (1998) demonstrated that for single microtubules, speckle appearance and disappearance indicate assembly and disassembly of the polymer. Using our framework for FSM simulations (see Materials and Methods), we learned that this is not true for actin meshworks, where fluorophores forming one speckle can belong to several crisscrossed filaments. A new speckle appears wherever the fluorophore distribution increases in number relative to the immediately adjacent surroundings. This can occur in two ways (Fig. 5): 1), new fluorophores are incorporated into the meshwork, resulting in a locally higher fluorophore density and giving rise to a new speckle; and 2), in an area with a low variation in fluorophore density and therefore no discernible speckles, the dissociation of fluorophores can result in a change of distribution such that the concentration of fluorophores becomes higher in one place compared to its surroundings. This may give rise to a new speckle as well. In the same manner speckles can disappear: either by dissociation of fluorophores at the site of the speckle, or by association of fluorophores in the neighborhood, resulting in a homogenization of the fluorophore distribution. Therefore, the algorithm has to distinguish between four situations (Fig. 5): *a*), speckle birth due to polymerization; *b*), speckle birth due to depolymerization; *c*), speckle death due to depolymerization; and *d*), speckle death due to polymerization). The graphs display the speckle and background intensity development from one time point before appearance until one time point after disappearance. The relevant event (birth or death) is marked with an arrow. As in Fig. 3 *d*, the confidence intervals for ΔI are plotted in the midpoints between the peak and background intensities.

Whether birth or death is associated with local assembly or disassembly of the actin meshwork can be decided based on the speckle intensity change in small time windows around the events. For all speckles with a lifetime of at least two time points, we consider the last time point ($t_b - 1$) before speckle appearance, the time point of appearance (t_b), and one time point after appearance ($t_b + 1$) (Fig. 5, *a* and *b*). Speckle and background intensities for the time point before appearance are extracted from the corresponding set of weak local maxima $L_N(t_b - 1)$. If an element of $L_N(t_b - 1)$ exists in the immediate spatial neighborhood of a speckle appearing at time t_b, then its intensity as well as the intensity of its background are added to the speckle history as the pre-birth event. If no such local maximum is found, the coordinates of the speckle and of the three local minima in t_b are used to obtain an estimate of the same values in $t_b - 1$. In the same way we consider the time point before ($t_d - 1$), at (t_d), and after speckle disappearance ($t_d + 1$) to classify the speckle deaths (Fig. 5, *c* and *d*). Fig. 5 *d* refers to a case of speckle death due to polymerization. The intensity development of this speckle demonstrates at the same time a pathological situation, sometimes occurring with the above explained extrapolation of intensities of pre-birth and post-death events. The birth of this speckle is characterized by a pre-birth difference between peak and background intensity larger than the confidence interval ΔI_C (*arrowheads*). Such a situation can only occur when no weak local maximum is available for extrapolation of the intensities in $t_b - 1$. The values for peak and background intensities are therefore extracted from the image using the coordinates of the speckle in t_b as explained before. In some cases, the intensity development between two consecutive time points can change abruptly, so that local intensity values get decorrelated over time. Any kinetic analysis in this time point is meaningless.

For the classification of a birth or death event, the speckle intensities as well as the background intensities at the time points around the actual event are fitted with linear regression. This yields an estimate of the rate of intensity change, represented by the slopes $a_{speckle}$ and $a_{background}$. We also calculate the standard deviation of the slopes using error propagation of the residuals of the intensity values to the

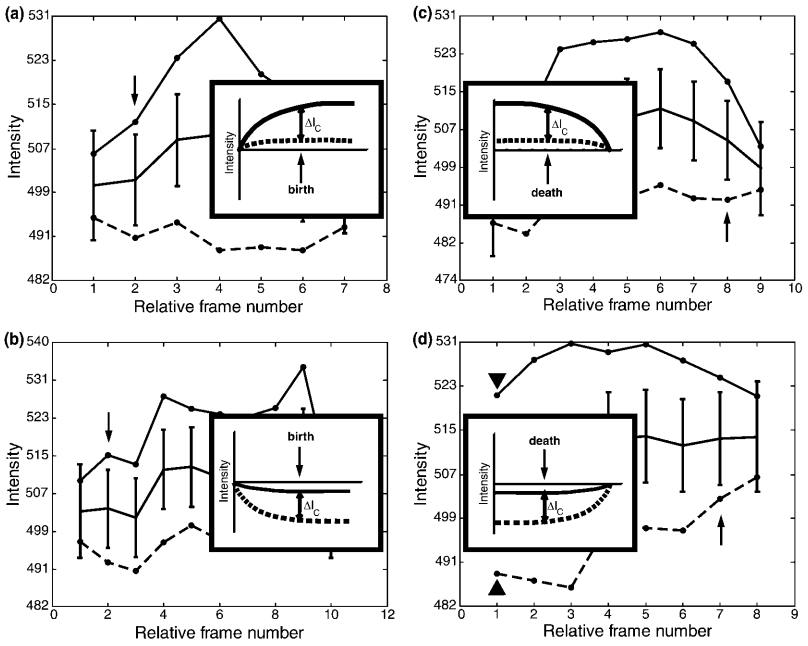

FIGURE 5 Classification of births due to polymerization (*a*) and births due to depolymerization (*b*), respectively; deaths due to depolymerization (*c*); and deaths due to polymerization (*d*). See text for further explanation of the scheme.

regression line. Noisy data, poorly represented by the linear model, will therefore generate large values for σ_a; intensity values in perfect match with the linear trend will result in small values for σ_a. We test the ratio $|a|/\sigma_a$ in a Student's *t*-test and exclude statistically insignificant slope measurements if $|a|/\sigma_a < Q_\alpha$. Then, we compare the ratios between speckle slope and background slope. Table 1 summarizes the conditions for each of the four event classes. The events which do not satisfy the criteria in Table 1 are excluded from the analysis.

It should be noticed that the strategy of analyzing only short intervals renders the algorithm relatively robust against the longer term effects of bleaching and intensity changes associated with focus drift or sample movement in axial direction.

Kinetic analysis of birth and death events and accumulation of actin turnover maps

Using the classification of speckle birth and death events, the final step of the algorithm is to extract a measure for the polymer kinetics reported by the speckle activity. This analysis is motivated by the fact that the changes in fluorescence intensity, which either lead to the formation or dissolution of a speckle, reflect, on average, the rate difference between local monomer association and dissociation. Nominally, the conversion factor between the rate difference and the observable intensity fluctuation is governed by the labeling ratio *f*. Of course, the same argument holds for any image point and not only for speckles. However, the appearance or disappearance of a speckle marks spots of particularly high kinetic action, which can be quantified significantly above noise, whereas the continuous analysis of a more homogeneous fluorescence signal over time is prevented by imaging artifacts such as noise and bleaching (see Discussion).

During classification, each significant event is assigned with the intensity slope $|a|$ resulting in the highest ratio $|a|/\sigma_a$. We refer to this slope as the score *s* of the event. Scores are counted positive for polymerization events and negative for depolymerization events (see last column of Table 1). Notice that the score values are highly stochastic: given a rate difference *r*, i.e., the net number of monomers

TABLE 1

Event	Class	Conditions			Ordered kinetics	Score *s*
Birth	Birth due to (speckle) polymerization	$a_{\text{speckle}} > 0$	$\frac{\lvert a_{\text{speckle}}\rvert}{\sigma_{a_{\text{speckle}}}} > \frac{\lvert a_{\text{background}}\rvert}{\sigma_{a_{\text{background}}}}$	$\frac{\lvert a_{\text{speckle}}\rvert}{\sigma_{a_{\text{speckle}}}} > Q_\alpha$	Polymerization	$s = a_{\text{speckle}} > 0$
	Birth due to (background) depolymerization	$a_{\text{background}} < 0$	$\frac{\lvert a_{\text{speckle}}\rvert}{\sigma_{a_{\text{speckle}}}} < \frac{\lvert a_{\text{background}}\rvert}{\sigma_{a_{\text{background}}}}$	$\frac{\lvert a_{\text{background}}\rvert}{\sigma_{a_{\text{background}}}} > Q_\alpha$	Depolymerization	$s = a_{\text{background}} < 0$
Death	Death due to (speckle) depolymerization	$a_{\text{speckle}} < 0$	$\frac{\lvert a_{\text{speckle}}\rvert}{\sigma_{a_{\text{speckle}}}} > \frac{\lvert a_{\text{background}}\rvert}{\sigma_{a_{\text{background}}}}$	$\frac{\lvert a_{\text{speckle}}\rvert}{\sigma_{a_{\text{speckle}}}} > Q_\alpha$	Depolymerization	$s = a_{\text{speckle}} < 0$
	Death due to (background) polymerization	$a_{\text{background}} > 0$	$\frac{\lvert a_{\text{speckle}}\rvert}{\sigma_{a_{\text{speckle}}}} < \frac{\lvert a_{\text{background}}\rvert}{\sigma_{a_{\text{background}}}}$	$\frac{\lvert a_{\text{background}}\rvert}{\sigma_{a_{\text{background}}}} > Q_\alpha$	Polymerization	$s = a_{\text{background}} > 0$

added or removed in the diffraction-limited area of a speckle, the variation of the score is proportional to $\sigma_S^2 \propto r \cdot f(1-f)$. In addition, the score measures are perturbed by noise according to Eq. 2. However, given a space-time window in which the rate difference r remains constant, statistical elimination of the score variation and noise perturbation is achievable by averaging the scores of several events. In this case, the expectation value is $\mu = r \cdot f$ for which the mean value of the scores $\bar{s}$ represents an unbiased estimator. In practice, these assumptions will not be completely satisfied: 1), the scores are susceptible to in- and out-of-focus movements of the entire sample, as well as of individual speckles; and 2), they are susceptible to bleaching. Artifacts due to single speckle axial motion are largely eliminated by averaging (see Discussion for a more detailed analysis of artifacts).

In summary, the kinetic analysis has to make a trade-off between robustness of the estimate and reduction in temporal and spatial resolution. The larger the space-time window, the less is the influence of the various perturbation factors, at the cost of lower density information. The second point to notice is that the scores can currently not deliver absolute rate values, but only relative values. To achieve absolute values one needs: 1), to have experimental control over the fraction f; and 2), to calibrate the conversion factor between fluorophore density and image signal intensity. Both requirements are practically difficult to fulfill with sufficient accuracy. Therefore, we confined the algorithm to kinetic mapping on a relative scale.

In the following, we explain the method for space-time averaging and simultaneous interpolation of the scores. Given the set of events $E(t) = \{e_1^t, \ldots, e_{n_t}^t\}$, $E(t-1) = \{e_1^{t-1}, \ldots, e_{n_{t-1}}^{t-1}\}$, $E(t+1) = \{e_1^{t+1}, \ldots, e_{n_{t+1}}^{t+1}\}$ at the time points t, $t-1$, and $t+1$, with the associated sets of event positions $P(t) = \{\mathbf{p}_1^t, \ldots, \mathbf{p}_{n_t}^t\}$, $P(t-1) = \{\mathbf{p}_1^{t-1}, \ldots, \mathbf{p}_{n_{t-1}}^{t-1}\}$, $P(t+1) = \{\mathbf{p}_1^{t+1}, \ldots, \mathbf{p}_{n_{t+1}}^{t+1}\}$ and scores $S(t) = \{s_1^t, \ldots, s_{n_t}^t\}$, $S(t-1) = \{s_1^{t-1}, \ldots, s_{n_{t-1}}^{t-1}\}$, $S(t+1) = \{s_1^{t+1}, \ldots, s_{n_{t+1}}^{t+1}\}$, we define for the time point t a score matrix $\mathbf{S}(\mathbf{x},t)$ of the same dimensions as the original image:

$$\mathbf{S}(\mathbf{x}_i, t) = \sum_{k=-1,0,1} \begin{cases} \omega^{|k|} \cdot s_i^{t+k}, \mathbf{x}_i \in P(t+k) \\ 0, \mathbf{x}_i \notin P(t+k) \end{cases}. \quad (5)$$

The parameter $k = -1, 0, 1$ defines the time offset around the central time point t. The weight function between the central time point and the previous and subsequent time points is set to $\omega = 1/e$. In other words, Eq. 5 corresponds to an accumulation of all event scores in a time stack, followed by Gaussian filtering, i.e., discrete convolution, along the time axis subject to negligence of filter values smaller than $1/e$. The additional low-pass filtering and hence reduction of resolution in the time domain is minimal. Already the score values at time t are extracted based on line regression of data from one time point before and after t. By applying Eq. 5, we therefore add only a small indirect coupling of the kinetic measures in t with those in $t-2$ and $t+2$.

Finally, spatial averaging is achieved for every time point by convolving

$$\mathbf{K}(\mathbf{x}, t) = \mathbf{S}(\mathbf{x}, t) * \mathbf{G}(r, d_0) \quad (6)$$

with a Gaussian kernel according to Eq. 1. The parameter d_0 is chosen adaptively as the mean distance between adjacent nonzero score values in any of the stack layers $\mathbf{S}(\mathbf{x}, t)$, $\forall t$. This means that the convolution kernel acts as a smooth transient between weighted averaging and interpolation. In areas with a high score density, i.e., several values fall inside the circle with radius d_0, the convolution takes the role of averaging resulting in more robust kinetic estimates, whereas in areas with only a few scores, the kinetic estimates are mainly obtained from interpolation between the nearest score values. If the distances to the nearest score value become larger than $3 \cdot d_0$, the kinetic estimate tends to zero, in correspondence with the infrequent occurrence of speckle birth and death events in such areas. $\mathbf{K}(\mathbf{x}, t)$ provides a continuous and smooth representation of the kinetic activity, and can be employed for further biological analyses (see Results). For display purposes, the values in $\mathbf{K}(\mathbf{x}, t)$ are binned into 31 score classes and are stored in a display stack, $\mathbf{D}(\mathbf{x}, t)$. The class boundaries were derived from several actin FSM movies, imaged under various experimental parameters. We extracted the range of practically relevant scores and divided it into 31 classes, symmetrically distributed around zero. Graphically, they are presented in color with colors ranging from green to dark blue for depolymerization, and from yellow to bright red for polymerization (see, e.g., color bar in Fig. 7 *c*).

RESULTS

Verification of the algorithm on synthetic data

To prove consistency and stability of the algorithm, it was first tested on synthetic data. Our FSM simulation package allowed us to generate synthetic movies where speckle intensity fluctuations were related to the kinetic activity of a Monte Carlo model of an actin meshwork (see Materials and Methods). The software also integrates imaging parameters, including models for image dark and shot noise, which we could freely turn on and off.

Fig. 6 shows the result of such a test. All our synthetic data was analyzed at a 95% confidence level. A homogeneous intensity field of $10 \times 10\ \mu m^2$ was divided into four subregions of which each was assigned to a different net assembly rate. The net assembly rate is defined by

$$r = [e^+]_A \cdot (k_{on}^+ \cdot M - k_{off}^+) + [e^-]_A \cdot (k_{on}^- \cdot M - k_{off}^-), \quad (7)$$

where $[e^+]_A$ and $[e^-]_A$ denote the area concentrations of the plus (barbed) and minus (pointed) actin filament ends, $k_{on}^{+/-}$ and $k_{off}^{+/-}$ are their respective association and dissociation rate constants, and M is the concentration of free actin monomers. The initial intensity was set in the range we

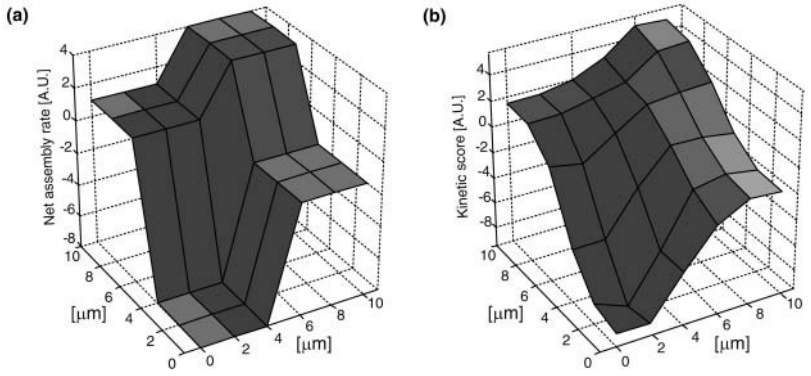

FIGURE 6 Speckle analysis on synthetic data. Synthetic FSM movies were created based on a model of meshwork assembly and disassembly and well-defined labeling ratios and optical parameters. (*a*) Net assembly rates (negative values denote disassembly) applied to generate synthetic 10×10 μm^2 FSM image stacks. (*b*) The normalized kinetic scores accurately match the input net assembly rates, except for smoothing due to averaging effects in the analysis.

usually get from experimental data, assuming uniform spatial distribution of label. The artificial meshwork was then allowed to polymerize and depolymerize according to the local net assembly rate.

Fig. 6 *a* shows the reference net assembly rates on a relative scale, where negative values denote disassembly. The output scores calculated by the algorithm are presented in Fig. 6 *b* on the same relative scale. The reference assembly rates and the output kinetic scores are in good agreement. This confirms the following three properties of the algorithm: i), in the chosen 95% confidence level, speckles are properly distinguished from intensity variations due to noise (see Algorithm—Statistical selection of speckles); ii), the classification of speckle birth and death events correctly distinguishes between assembly and disassembly (see Algorithm—Classification of birth and death events); and iii), despite their inherently stochastic nature, the slopes of the intensity profiles around birth and death reflect, on average, the local kinetic property of the meshwork on a linear, relative scale (see Algorithm—Kinetic analysis).

The scores at the boundaries between the four subregions are not sharply defined as the input data. This is due to low-pass filtering in the time and space domain, necessary to average the scores of several events. The graph suggests that the spatial resolution of our analysis is in the range of 1–2 μm given input data using a pixel size of 67 nm expressed in object domain and a 100×/1.4 NA optics.

FSM analysis of cortical actin meshworks reveals cyclic polymer turnover

After initial validation, the software was applied to data from live cell experiments. We imaged and analyzed the cortical regions of contact-inhibited newt lung epithelial cells using a spinning-disk confocal microscope system equipped with a cooled CCD detector (see Materials and Methods). X-rhodamine-labeled actin was microinjected into contact-inhibited cells in the interior of a monolayer sheet of epithelial cells and 600×600 pixel^2 images were acquired at 5-s intervals. Oxyrase was added to reduce photobleaching effects (Waterman-Storer et al., 1993; Mikhailov and Gundersen, 1995). Fig. 7 shows the turnover in the cortical actin at the ventral cell surface, as revealed by our software. The overall distribution of fluorescent actin in the edge region of a cell is shown in Fig. 7 *a*. Note that the cell is in contact with an adjacent cell (*top black region*) that had not been labeled with fluorescent actin. The region overlaid by a white box indicates the area analyzed in Fig. 7 *b*, which presents eight consecutive time frames at 5-s intervals of a kinetic map generated by our algorithm. The color coding is illustrated by the scale bar in Fig. 7 *c*. Strong polymerization corresponds to dark red, strong depolymerization to dark blue.

Although there is an overall equilibrium of polymerization and depolymerization, our analysis reveals alternating polymerization and depolymerization waves in spatially discrete cellular regions. These oscillatory kinetics are illustrated at the positions indicated with an arrow and an arrowhead, respectively. Both positions show a cyclic behavior between states of prevalent polymerization turning into states of depolymerization with subsequent recovery of polymerization. For a position close to the junction with the adjacent uninjected cell (Fig. 7 *b*, *arrowhead*), the meshwork starts in a state of moderate depolymerization, which gets stronger at time point 225 s, weakens again at 230 s, and turns into weak polymerization at 235 s. Polymerization peaks 10 s later before it weakens again and finally returns in a state of depolymerization (255 s). The position pointed out with the arrow exhibits a similar cycle but starts with weak polymerization.

We conclude that the cortex is divided in small subareas of the size of a few μm^2, which polymerize and depolymerize in phase-shifted cycles of similar periodicity. Qualitatively, a similar cyclic behavior can be observed in time-lapse phase-contrast microscopy of contact-inhibited cells in the form of spatial waves in the intensity signal (data not shown). However, the underlying physiological effect was hitherto unclear.

In Fig. 7 *d*, we further analyze the cycling in three 2.5×2.5 μm^2 regions indicated in Fig. 7 *a* with a red, a blue, and a green box. Independent of the cellular position, the meshwork cycles with a period in the range 35–45 s. Fig. 7 *e*

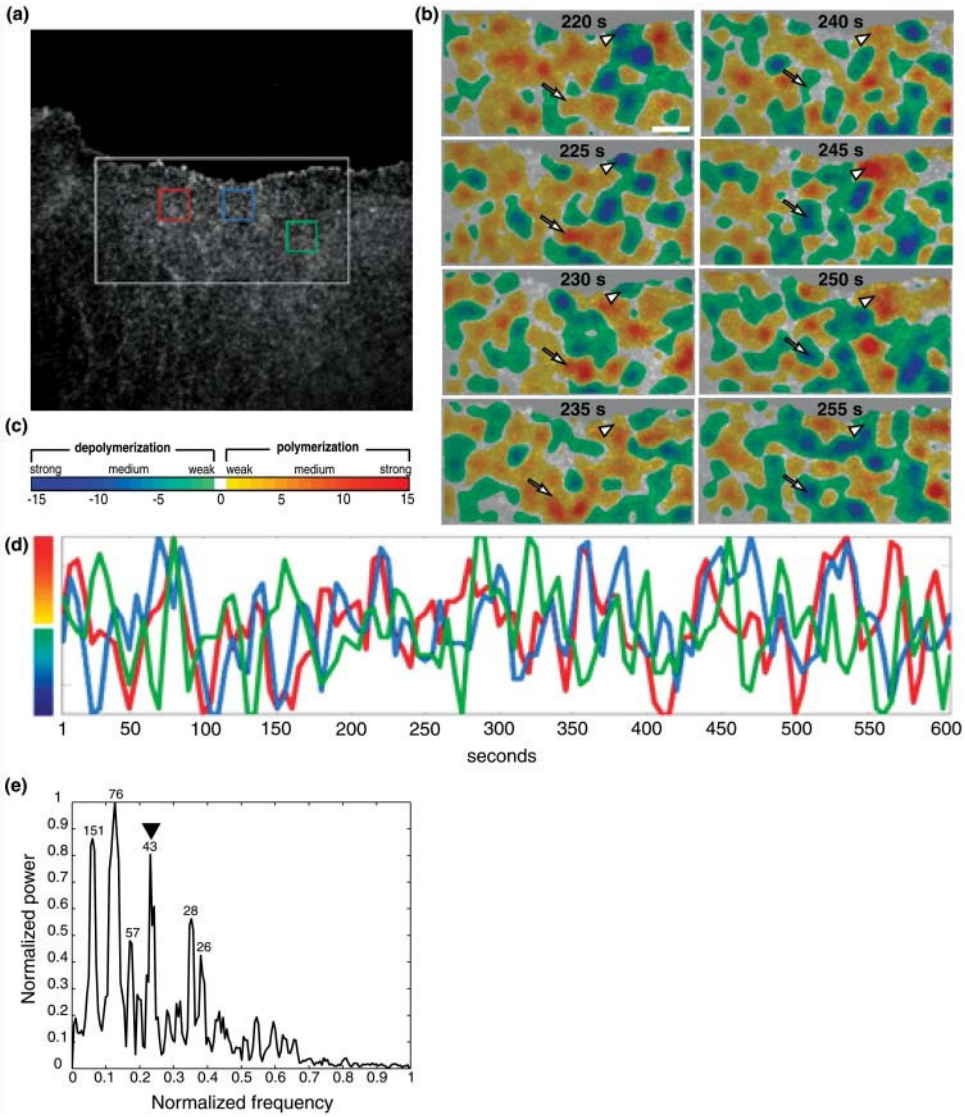

FIGURE 7 FSM analysis of F-actin turnover in the lamellipodium of a newt lung epithelial cell. (*a*) Overview of the cell area imaged by FSM. The kinetic analysis displayed in *b* refers to the region delimited by the white frame. (*b*) Eight panels showing kinetic maps over a period of 35 s, starting at time point 220 s. Two positions are selected to indicate the periodic cycling of the actin meshwork. The arrowhead points to a region cycling from depolymerization to polymerization back to depolymerization. The arrow points to a region where the cycle is 180° phase-shifted. Scale bar, 2.5 μm. (*c*) The color map used for displaying 31 score classes in the kinetic maps. (*d*) The mean kinetic score per unit time and area (2.5 × 2.5 μm^2) over 600 s for three selected regions (see *colored boxes* in *a*) reveals a space-independent cycling rate of ~40 s^{-1}. (*e*) Overall power spectrum of the cycles in *d*. The spectrum has three predominant peaks, corresponding to cycling periods of 151 s, 76 s, and 43 s. They are approximately in an octave ratio to one another. A second pair found in the data are the 26- and 28-s periods in octave to the 57-s cycle.

underlines this observation with a power spectrum of actin kinetic cycling. The spectrum has three predominant peaks, corresponding to cycling periods of 151 s, 76 s, and 43 s. Notice that the first two cycles are almost octave matches to the cycle with the 43-s period. Therefore, they are relatively difficult to observe in the direct spaces revealed by the map in Fig. 7 *b* and the graph in Fig. 7 *d*. In addition, the spectral analysis of Fig. 7 *e* reveals a second octave pair of frequencies in the turnover cycling (26 s and 28 s, which match approximately with the 57-s cycle). Interestingly, such cycling has also been observed in the context of lamellipodial protrusion in fibroblasts (Ballestrem et al., 2000). Kymograph analyses of a free leading edge exhibited a transient ruffling at a cycling period of 40–50 s, hence in almost perfect agreement with our result. We may conclude that under similar physiological conditions, the steady state of an actin meshwork is characterized by an oscillatory turnover, which results in cells with a free leading edge in lamellipodial protrusion and retraction, whereas in contact-inhibited cells this behavior causes assembly and disassembly of the cortical actin cytoskeleton without cell morphological consequences.

To verify that the discovered cycling phenomenon is indeed a physiological effect and not an artifact of the analysis, we used our simulation framework to generate steady-state conditions, i.e., for any time interval in the simulation, the number of monomers added and removed from a spatial unit was equal. The analysis of such data reported zero activity, as expected (results not shown). In addition, we simulated data where the meshwork was subjected to constant net polymerization, and to kinetics with phases of net polymerization and depolymerization alternating in periods of 9 s (Fig. 8). The insets of Fig. 8, *a* and *b*, show the evolution of the simulated net polymerization rate throughout the two test experiments. Fig. 8 *a* shows the power spectrum in the case of constant polymerization. As expected, the spectrum

concentrates at the zero frequency (DC). In contrast, the power spectrum of Fig. 8 *b* contains a strong peak at a frequency $1/9\,s^{-1}$, in precise match with the predefined cycling rate between assembly and disassembly of the second simulation. The small fluctuations besides the dominating peaks in both spectra underline again that speckles are a stochastic signal generating various side frequencies, even when the signal represents the outcome of a perfectly deterministic turnover. To conclude, these tests confirm that our algorithm is indeed capable of reporting kinetic events that occur in regular cycles, suggesting that the results in Fig. 7 *e* are very likely to reflect a hitherto unknown behavior of F-actin meshworks.

Latrunculin-A perfusion induces a spreading of the cycle frequencies

To study if external perturbations of the actin meshwork activity could be tracked by our algorithm, injected cells were perfused with latrunculin A, a drug known to disrupt the actin cytoskeleton in several mammalian nonmuscle cells (Spector et al., 1983). The suggested model of latrunculin A binding to G-actin monomers to form a stoichiometric 1:1 complex (Yarmola et al., 2000) has recently been modified by Pring et al. (2002), who suggest the existence of a yet unknown species that participates in the formation of a ternary complex with latrunculin A and G-actin. This puts the effects of latrunculin A into a more complicated context that can eventually be resolved by FSM assaying. Here, we focus on our first observations.

We used a low dose (750 nM) of the drug to prevent catastrophic depolymerization of actin and major morphological changes, which both would have biased our FSM analysis. We expected that a low dose would suffice to shift the cyclic steady state toward actin filament disassembly, or at least to perturb the meshwork cycling. Contact-inhibited cells were first imaged under control conditions (Fig. 9 *a*—before latrunculin-A perfusion) and our analysis software revealed similar behavior as in Fig. 7 *e*, with discrete regions showing cycling between polymerization and depolymerization of ~166 s (Fig. 9 *b*). Notice that each of the frames in Fig. 9 shows the score integrated over a 50-s period, i.e., cycle rates faster than 100 s are deliberately obscured. Detailed spectral analysis for this experiment reveals similar peak frequencies as in Fig. 7 *e*, supporting our speculation about a universal rule for steady-state actin turnover under comparable physiological conditions.

In the first panel (50 s) after perfusion of latrunculin A, the tendency for polymerization from the last panel before treatment of the cell continues. Only the second panel after perfusion shows a strong homogenous depolymerization, which is succeeded by continuously stronger repolymerization already one or two panels (50–100 s) later. This means that the system undergoes a relatively rapid recovery. Unfortunately, it was impossible to analyze the cells for more than 200 s because latrunculin A induces cell rounding. Nevertheless, the high sensitivity of our algorithm allowed us to uncover an unexpected effect of latrunculin A treatment. Fig. 9 *c* displays the power spectrum of cyclic actin turnover after perfusion. The drug shifts the cycling toward more and higher frequencies. Notice that the DC values of both spectra 9 *b* and 9 *c* are almost zero, indicating that there is no average tendency for either meshwork assembly or disassembly. In other words, the application of low doses of latrunculin A does not simply cause net depolymerization, but the meshwork reacts with a rapid and sustained repolymerization in many and fast cycles. This can be interpreted as a perturbation leading to higher disorder of the system.

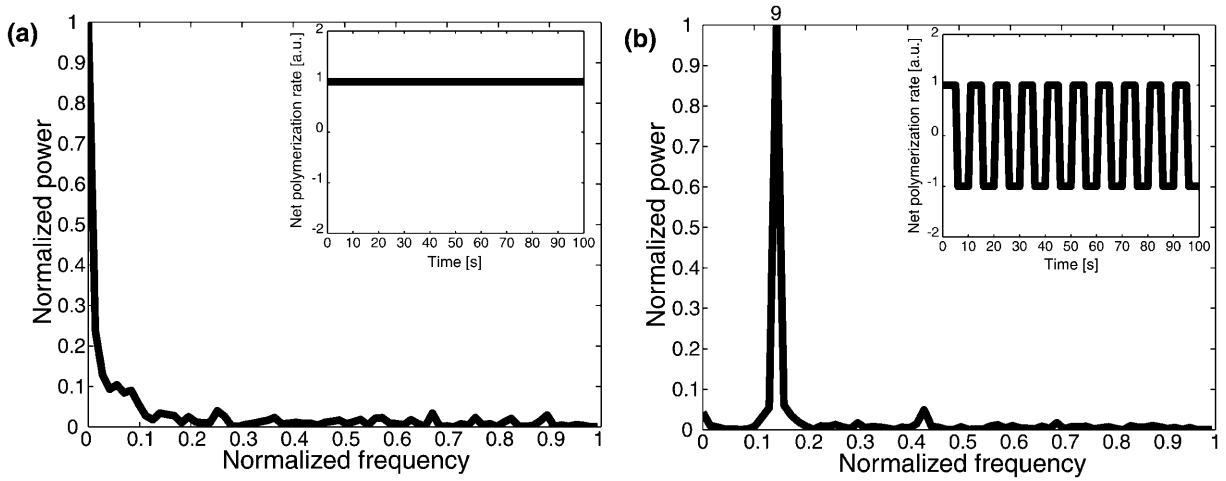

FIGURE 8 Power spectra of synthetic data. (*a*) Analysis of a meshwork with constant net polymerization (*inset*). The spectrum is concentrated in the zero (DC) frequencies. (*b*) Analysis of a meshwork with alternating phases of net assembly and disassembly with a period of 9 s. Here, the spectrum concentrates in a peak at the corresponding frequency.

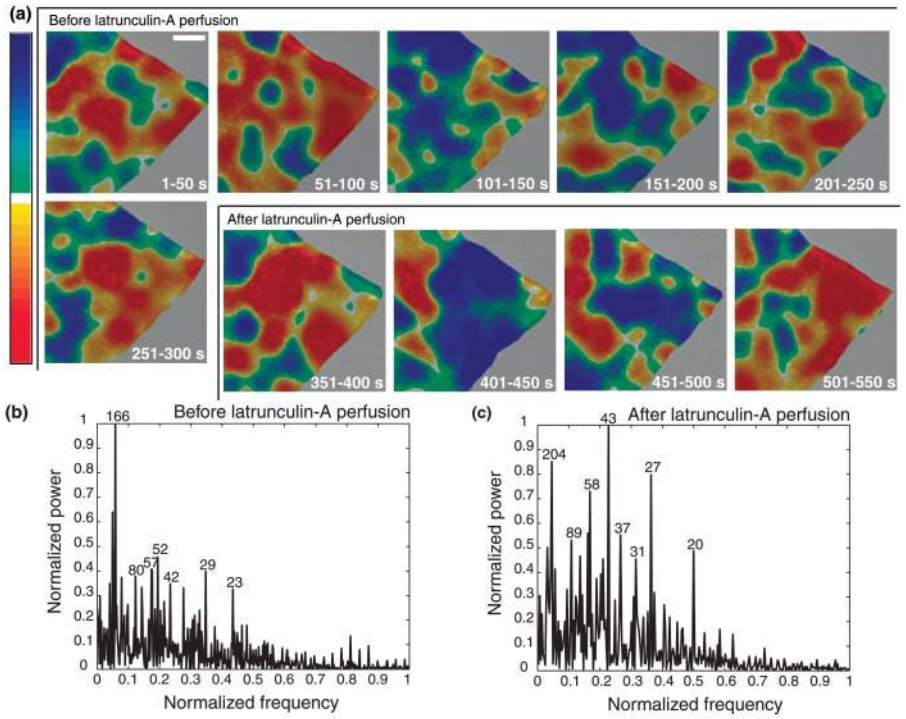

FIGURE 9 F-actin turnover after latrunculin-A perfusion. Cells were first imaged during 300 s under control conditions and then perfused with 750 nM of latrunculin A. (*a*) Frames showing the scores integrated over a period of 50 s. Scale bar, 2.5 μm. Comparison of the power spectra before (*b*) and after (*c*) latrunculin-A perfusion.

DISCUSSION

FSM analysis relies on a statistical separation of significant events

In this paper we introduce an algorithm for automated analysis of the assembly and disassembly kinetics of actin meshworks from fluorescent speckle microscopy movies of living cells. As discussed in the outline of the Algorithm, speckles represent an inherently stochastic and very dynamic signal perturbed by likewise stochastic noise. The core of information extraction from speckle data, therefore, relies on the statistical separation of two stochastic signal components, followed by time- and space-averaging of the component associated with the speckle signal. This reveals statistical trends describing the kinetics of monomer association and dissociation to and from a polymer structure.

The separation of the speckle signal from noise requires modeling the characteristics of both signal components. For the speckle signal we know that it represents a diffraction-limited image of local peaks in fluorophore concentration, which is accounted for by the initial low-pass filtering. The further separation is based on a model of image noise. Three parameters have to be set that are the proportionality factor β for shot-noise dependence in image intensity, the dark noise variance α_{DN}, and the mean intensity of the dark field (see Eq. 2). The first parameter β has been calibrated once for all relevant exposure times and thus is stored in a software look-up table. The second and third parameters vary between experiments. They must be calibrated for every image series, for which the software operator has to select a small window devoid of speckles. The only parameter that requires manual input is the confidence level α on which all the statistical tests are performed. However, the setting of this parameter is also unproblematic. The statistical selection processes turn out to be very robust for confidence probabilities between 80% and 99% (also see Fig. 12 below). Based on these parameters, the algorithm performs three essential steps (see Fig. 2): i), statistical selection of speckles; ii), statistical classification of speckle birth and death events to ascertain meshwork polymerization and depolymerization; and iii), statistical analysis of the intensity development in these events. Time changes in the intensity are, on average, related to the kinetics of monomer association and dissociation.

In a recent paper, Watanabe and Mitchison (2002) used single-fluorophore FSM to quantify F-actin flow and meshwork activity in lamellipodia of fibroblasts. They tracked a few selected speckles by hand and performed statistical analysis on the lifetime and movement of the speckles. In analogy to the present work, single-fluorophore speckle appearances and disappearances served as local reporters of meshwork turnover. Single-fluorophore FSM has the advantage that every labeled monomer added to the meshwork results in a new speckle, and dissociation of a labeled monomer removes a speckle. Consequently, in this kind of data the speckle lifetime is a direct measure of the kinetic activity. However, single-fluorophore FSM also has disadvantages: i), besides the experimental challenges of stably imaging single fluorophores, the labeling ratio has to be kept extremely low with the result that the speckle distributions are low density and thus provide limited spatial sampling; ii), the

SNR is weak, which requires long exposure times and thus limits the temporal resolution; and iii), the speckle appearances and disappearances deliver only binary information, comparable to an on/off switch. To convert this binary data into smooth kinetic rate measures requires substantial averaging in space and time over several speckles, which lowers the resolution of the method further. It is an open question whether single fluorophore speckles could characterize the dynamic equilibrium of a spatially stationary meshwork as reported by Fig. 7, where polymerization and depolymerization coexist in very close proximity, and whether it has sufficient temporal resolution to extract the short-term fluctuations of the equilibrium.

In our multifluorophore approach, speckles are the result of local clustering of several monomers, perhaps in different filaments within the volume of the PSF. Speckle births and deaths result from a significant change in the local number density of labeled monomers. As discussed in the section Algorithm—Kinetic analysis, the score of an event corresponds to the slope of either the peak or background intensity development, and therefore is a direct measure of the temporal change of the number of labeled monomer at the position of the speckle. Our score delivers more continuous information than the binary answer of a single-fluorophore speckle, and allows us to distinguish with one measurement between a slow and a fast process. Averaging is still necessary for elimination of the inherent variation of the score values, but we believe that much fewer speckles are necessary to obtain a robust kinetic rate estimate.

The effect of bleaching on FSM analysis is minimal and can be eliminated completely by an appropriate correction scheme

To test the robustness of the algorithm against imaging artifacts, we examined the effect of intensity changes due to photobleaching. We performed two experiments on cells that were fixed 1 h after microinjection with labeled actin. During this time, the labeled actin was allowed to incorporate into filaments until the equilibrium between free monomers and filaments was established. In fixed cells, no actin meshwork activity is supposed to occur. The two protocols differed in the strength of illumination and the use of antifading agents. As with all our experimental data, the confidence level α was set to 95% for both experiments.

Both actin disassembly and photobleaching lead to a decrease of labeled monomer and thus we expect the software to have its report biased toward depolymerization. In the first experiment, the fixed cells were imaged under strong illumination conditions. The exposure time was set to 10 s and no antifading agents were applied. Strong bleaching was the result and we expected the software to return kinetic maps indicating mostly depolymerization. This is largely confirmed by Fig. 10 *a*. Most parts of the cortical meshwork show strong depolymerization, with the exception of one region where the reported trend is the opposite. A thorough analysis of the raw FSM movie revealed that in this area new speckles occurred with an increasing absolute peak intensity (data not shown). At the moment the origin of this imaging artifact is unclear.

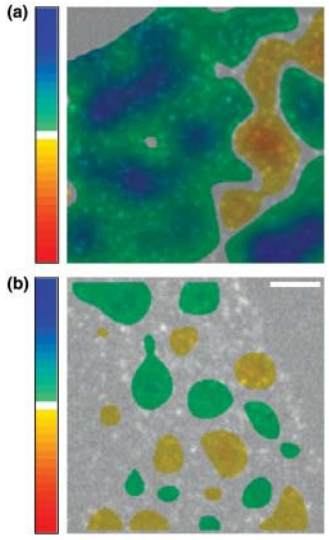

FIGURE 10 Effects of intensity changes due to photobleaching tested on fixed newt lung epithelial cells with a speckled actin cytoskeleton. (*a*) An exposure time of 10 s per image induced strong bleaching represented by green to dark-blue areas. (*b*) An exposure time of 5 s and the addition of Oxyrase as an antifading agent reduced the bleaching dramatically. Scale bar, 2.5 μm.

Fig. 10 *b* shows the analysis of an experiment with more moderate exposure times and where Oxyrase was added to reduce bleaching. The exposure time was set to 5 s, which is still higher than the 2–3.5 s of our live cell imaging protocol. Again, depolymerization as well as some artifactual polymerization events are reported by the software. Notice, however, the large reduction of the scores as compared with the first experiment. This indicates that the majority of the map in Fig. 10 *a* is indeed associated with fluorophore bleaching. The scores cover only the lowest kinetic classes, which means that under regular exposure time and under the application of antifading agents, the effect of bleaching on FSM analysis is minimal.

Nevertheless, bleaching is a systematic effect and hence could be eliminated from the analysis by an appropriate correction scheme. To test the extent to which bleaching affects the analysis of live cell experiments, we analyzed the distribution of positive and negative scores from the weak bleaching experiment in comparison to the score of the data set shown in Fig. 7. Fig. 11 *a* shows the relative occurrences of bleach-induced scores (*red histogram*) overlaid to the scores measured in a live cell experiment (*blue histogram*). The two histograms clearly differ, which means that scores due to bleaching can be eliminated. Thus, we supplemented the algorithm with an entirely data-driven bleaching

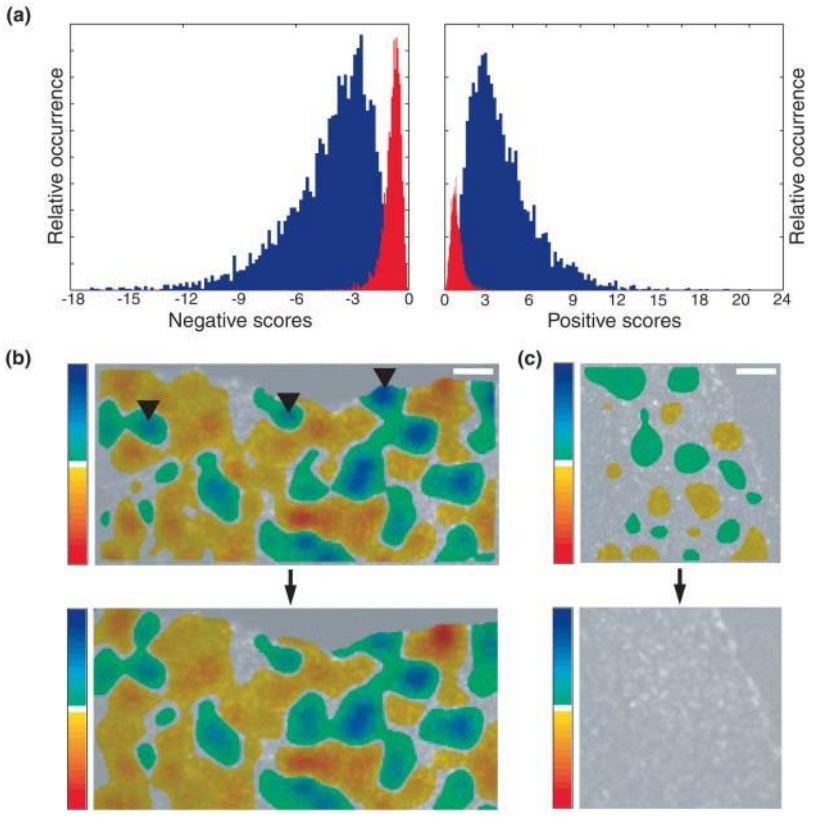

FIGURE 11 (*a*) Characterization of bleach-induced scores (*red*) relative to scores measured in live cell experiments (*blue*). The score distributions are clearly distinct, so that score biases due to bleaching can be compensated (see text for a description of the bleaching correction). (*b*) Bleaching correction applied to an uncorrected panel of Fig. 7 and (*c*) to Fig. 10 *b*. The maps show that the correction indeed eliminates the marginal bias induced by bleaching; however, it does not change the quality of kinetic maps from live cell experiments. The arrowheads in *b* indicate some depolymerization scores that are slightly diminished by the bleaching correction. Scale bars, 2.5 μm.

compensation module: from the modes of the two red histograms, the module automatically derives thresholds that discriminate weak scores due to bleaching from scores related to F-actin meshwork turnover. After removal of weak scores, the kinetic map is recalculated according to the filtering and interpolating scheme discussed in the section Algorithm—Kinetic analysis. Fig. 11, *b* and *c*, display the effect of such correction. In agreement with the conclusions above, changes in the map due to the bleaching correction are very minimal and almost only visible for areas with strong depolymerization that get slightly diminished (*arrowheads* in Fig. 11 *b*). The reason for this minimal effect originates in the strategy of analyzing the speckle intensity development only over short time intervals around birth and death events. It implies that the intensity changes exploited are systematically severalfold larger than intensity changes associated with bleaching over such time spans. To demonstrate the self-consistency of the correction scheme, we display in Fig. 11 *c* a bleach-corrected version of the map in Fig. 10 *b*. Indeed, the scheme removes all scores from the map, indicating that our analysis correctly reports no meshwork activity for a fixed cell.

The effect of focus changes

In addition to intensity variations due to bleaching, focal shifts may mistakenly lead to false birth and death events. We can think of two types of focal changes. On the one hand, single speckle axial motions occur, which affect the intensity development of one speckle independent of any other speckle. They are a stochastical process on average leading to the same amount of birth and death events. Therefore, their contribution to the score cancels out by averaging. On the other hand, a coordinated axial shift of many speckles may occur. Origins of such motion are *z*-stage drifts and vertical movements of entire cell parts, as for example induced by contraction. The first problem could be reduced by means of sophisticated closed-loop stage controllers (Lanni, 1993), which were, however, not used for data acquisition in this paper. Unfortunately, the second problem is out of our experimental control.

To quantify the sensitivity of the algorithm to coordinated *z*-motion, images of fixed newt lung epithelial cells were acquired at 100 nm *z*-intervals using a stepper motor focus controller. These cells were not contact inhibited, as revealed by the presence of a large lamellipodium. In accordance with the parameters of live cell experiment, the exposure time was set to 3 s and Oxyrase was added to reduce photobleaching.

Fig. 12 *a* gives an overview, where the transition from the very thin lamellipodium to the thicker cell body is highlighted. The thickness of lamellipodial actin sheets has been quantified in the range of 200 nm by Abraham et al. (1999). Hence, we anticipate that 100-nm stage shifts have a significant effect on the scores in the lamellipodium, whereas the much thicker cell body should be more insensitive toward such shifts. Depending on the position

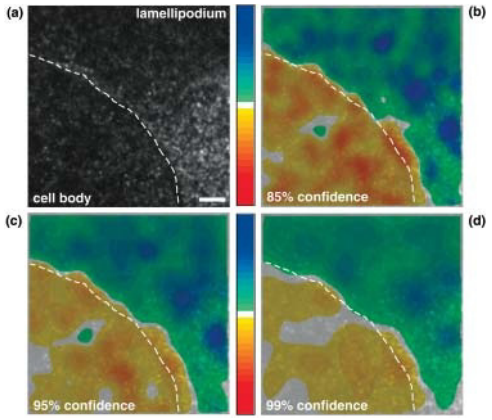

FIGURE 12 Characterization of kinetic scores induced by focal shifts. Fixed cells with a speckled actin cytoskeleton were imaged in a series, at 3-s exposure time and with Oxyrase added, where the focus was changed in steps of 100 nm between frames. (*a*) Overview of the cell indicating the transition between the thick cell body and the much thinner (~200 nm) lamellipodium. Panels *b–d* show the kinetic maps calculated at the confidence levels $\alpha = 85$, 95, and 99%. Scale bar, 2.5 μm.

of the focus plane relative to the heights of cell body and lamellipodium, a result like the one in Fig. 12, *b–d*, can be expected. The movement causes positive scores for the cell body (Fig. 12, *b–d*), where new speckles enter the focus plane, and negative scores for the lamellipodium, where a 100-nm step induces almost complete disappearance of all speckles. However, the drift effects are significantly lower for the cell body area, where a certain ''random symmetry'' in the vertical speckle distribution leads to an averaging effect. This becomes particularly obvious with alterations of the confidence probability. Fig. 12, *b–d*, illustrates the dependence of the scores on the choice of α. The higher the confidence, the lower is the risk of including artifactual events into the score analysis. At 99% confidence, scores for the cell body are almost exclusively in the two lowest score classes (*faint yellow*), whereas at 85% a considerable amount of false events is collected. Nevertheless, the series also indicates that the general trends of the maps are unaffected by the setting of the confidence probability and thus that the algorithm is very robust in reporting the main characteristics of polymer turnover.

We conclude from this data that uncontrolled focus drifts have a dramatic effect on the extraction of kinetic measurements. However, the drift rates applied to the data shown in Fig. 12 are far beyond what is encountered in live cell experiments. Such drifts have never been observed in real experiments, where an operator visually supervised the image acquisition and small focus corrections were applied manually approximately every 20–30 frames. There is a second reason why we believe that our live cell experiments are only minimally perturbed by focus drifts. As evident from Fig. 12, focus drifts cause coherent score drifts over large areas of the field of view. In none of our cell experiments have we observed such spatially homogeneous score maps, but the maps were always highly structured as in the data shown in Fig. 7. Finally, the data examined in Fig. 10 *b* contains, in a strict sense, a superposition of bleaching and focus drift effects, as these bleaching series were acquired in the same manner as any other data set, i.e., with manual compensation of focus drifts. With Fig. 11 we demonstrate that these biases can be appropriately eliminated.

Local meshwork contractions are most likely to result in ghost speckles, which are excluded from the analysis

There is a third potential source of error in our analysis originating in motor-induced local meshwork contraction. Although positional fluctuations of speckles induced by such contraction are properly accounted for (see Algorithm—Micromovement tracker), contraction and subsequent release of the meshwork can also cause the formation of new speckles and the dissolution, fusion, and splitting of existing speckles. In all of these situations, our software is likely to detect the birth or death of a speckle that is not associated to meshwork turnover. As with the axial motion of single speckles in and out of focus, these are stochastic events with zero mean score that average out by appropriate spatial and temporal filtering. The kinetic map in Fig. 7 suggests a cyclic turnover of actin with a cycling period of 30 s and more. Therefore, a time window of up to 15 s could be used to eliminate artifactual birth and death events from the analysis without obscuring the kinetic behavior of polymerization and depolymerization. As indicated by Eq. 5, our temporal averaging was more conservative. We limited the averaging to three time points in 5-s frame rate data, which corresponds to a time window of 10 s.

Our data provides clear evidence that contraction-related speckle appearances and disappearances even take place in rates much faster than with a period of 10 s. Besides the data presented in the Figures of this paper, which were consistently acquired at 5-s intervals between frames, we have also analyzed movies with frame rates of 1 s, 3 s, and 10 s. On the one hand we examined the number of ghost speckles as a fraction of the total number of extracted speckles. For all movies and independent of the frame rate, it was in the range 40–50%. We can exclude that these large numbers of ghost speckles are due to noise. All our images are carefully low-pass filtered, and speckles are subsequently selected on a confidence level between 80% and 99%, allowing a maximum of 20% insignificant local maxima that are falsely detected as speckles. Consequently, ghost speckles do represent a significant signal with a lifetime shorter than the currently achievable acquisition rate of 1 s. On the other hand, we compared the power spectra of polymer turnover between the movies and found no additional peak when increasing the frame rate, suggesting that indeed all

major polymerization-related cycles are retrieved by our computational analysis of 5-s data. We conclude that ghost speckles are not related to meshwork turnover and hence are likely the product of fast local meshwork contraction. There is further support for this argument by the fact that ghost speckles have, on average, an intensity 1.5–2.0 times lower than the intensities of speckles living over more than one time point. Even with only 1-s frame rate, the exposure time necessary for FSM image acquisition amounts to almost 1 s. Fast local meshwork movements induced by contraction would cause a smear of the signal that is in agreement with the observed intensity reduction. Since ghost speckles are not included in the score analysis, it seems very likely that our system is largely unaffected by the meshwork contraction. Nevertheless, an extended series of experiments with ATP depleted cells and controls with inhibitors of myosin activity and polymerization is planned for the future to provide a conclusive proof of this argument.

In summary, we have developed a completely automatic and robust software that maps the kinetics of spatially stationary F-actin meshworks in living cells injected with fluorescent actin and imaged by FSM, by analyzing every speckle as a local reporter of meshwork turnover. Applications of this novel quantitative FSM are manifold. They range from fundamental studies of polymer dynamics in situ, the analysis of mechanisms mediating cell migration and morphogenesis, to very sensitive high-content screening of drugs and regulators affecting the cytoskeleton dynamics. In the near future, we will combine this program with a module for tracking large-scale speckle movements, which will enable us to map cytoskeleton kinetics and translocation dynamics at the same time.

This work was supported by the Swiss National Science Foundation (21-59452.99) to G.D., the National Institutes of Health (GM 61804-01) to C.M.W.-S., and a collaborative Young Investigators Award from the Human Frontiers Science Programme to C.M.W.-S., G.D., and Inke Näthke (University of Dundee).

REFERENCES

Abercrombie, M., J. E. Heaysman, and S. M. Pegrum. 1972. Locomotion of fibroblasts in culture. V. Surface marking with concanavalin A. *Exp. Cell Res.* 73:536–539.

Abraham, V. C., V. Krishnamurthi, D. Lansing Taylor, and F. Lanni. 1999. The actin-based nanomachine at the leading edge of migrating cells. *Biophys. J.* 77:1721–1732.

Ballestrem, C., B. Wehrle-Haller, B. Hinz, and B. A. Imhof. 2000. Actin-dependent lamellipodia formation and microtubule-dependent tail retraction control-directed cell migration. *Mol. Biol. Cell.* 11:2999–3012.

Danuser, G., and R. Oldenbourg. 2000. Probing F-actin flow by tracking shape fluctuations of radial bundles in lamellipodia of motile cells. *Biophys. J.* 79:191–201.

Forscher, P., and S. J. Smith. 1988. Actions of cytochalasins on the organization of actin filaments and microtubules in a neuronal growth cone. *J. Cell Biol.* 107:1505–1516.

Harris, A. K. 1999. A dozen questions about how tissue cells crawl. *Biochem. Soc. Symp.* 65:315–341.

Lanni, F. 1993. Feedback-stabilized focal-plane control for light microscopes. *Rev. Sci. Instrum.* 64:1474–1477.

Maddox, P. S., B. Moree, J. C. Canman, and E. D. Salmon. 2003. A spinning disk confocal microscope system for rapid high resolution, multimode, fluorescence speckle microscopy and GFP imaging in living cells. *In* Biophotonics, Parts A and B. G. Marriott and I. Parker, editors. Academic Press, San Diego, CA. And *Methods in Enzymology.* 2003. Vol. 360. In Press.

Mikhailov, A. V., and G. G. Gundersen. 1995. Centripetal transport of microtubules in motile cells. *Cell Motil. Cytoskeleton.* 32:173–186.

Oshiro, M. 1998. Cooled CCD versus intensified cameras for low-light video—applications and relative advantages. *Methods Cell Biol.* 56: 45–62.

Papoulis, A. 1991. Probability, Random Variables, and Stochastic Processes, 3rd ed. McGraw-Hill International Editions, New York.

Pollard, T. D. 1986. Rate constants for the reactions of ATP-actin and ADP-actin with the ends of actin filaments. *J. Cell Biol.* 103:2747–2754.

Pring, M., L. Cassimeris, and S. H. Zigmond. 2002. An unexplained sequestration of latrunculin A is required in neutrophils for inhibition of actin polymerization. *Cell Motil. Cytoskeleton.* 52:122–130.

Reider, C. L., and R. H. Hard. 1990. Newt lung epithelial cells: cultivation, use, and advantages for biomedical science. *Int. Rev. Cytol.* 122:153–220.

Salmon, W. C., M. C. Adams, and C. M. Waterman-Storer. 2002. Dual-wavelength fluorescent speckle microscopy reveals coupling of microtubule and actin movements in migrating cells. *J. Cell Biol.* 158:31–37.

Small, V. 1981. Organization of actin in the leading edge of cultured cells. *J. Cell Biol.* 91:695–705.

Spector, I., N. R. Shochet, Y. Kashman, and A. Groweiss. 1983. Latrunculins: novel marine toxins which disrupt microfilament organization in cultured cells. *Science.* 214:493–495.

Wang, Y. L. 1985. Exchange of actin subunits at the leading edge of living fibroblasts: possible role of treadmilling. *J. Cell Biol.* 101:597–602.

Watanabe, N., and T. J. Mitchison. 2002. Single-molecule speckle analysis of actin filament turnover in lamellipodia. *Science.* 295:1083–1086.

Waterman-Storer, C. M. Fluorescent speckle microscopy (FSM) of microtubules and actin in living cells. Current Protocols in Cell Biology. J. S. Bonifacino, M. Dasso, J. B. Harford, J. Lippincott-Schwartz, and K. M. Yamada, editors. John Wiley & Sons, New York. 1:4.10.1–4.10.26.

Waterman-Storer, C. M., and G. Danuser. 2002. New directions for fluorescent speckle microscopy. *Curr. Biol.* 12:R633–640.

Waterman-Storer, C. M., A. Desai, J. C. Bulinski, and E. D. Salmon. 1998. Fluorescent speckle microscopy: visualizing the movement, assembly, and turnover of macromolecular assemblies in living cells. *Curr. Biol.* 8:1227–1230.

Waterman-Storer, C. M., and E. D. Salmon. 1997. Actomyosin-based retrograde flow of microtubules in the lamella of migrating epithelial cells influences microtubule dynamic instability and turnover and is associated with microtubule breakage and treadmilling. *J. Cell Biol.* 139:417–434.

Waterman-Storer, C. M., and E. D. Salmon. 1998. How microtubules get fluorescent speckles. *Biophys. J.* 75:2059–2069.

Waterman-Storer, C. M., and E. D. Salmon. 1999. Fluorescent speckle microscopy of microtubules: how long can you go? *FASEB J.* 13 (Suppl):S225–S230.

Waterman-Storer, C. M., W. C. Salmon, and E. D. Salmon. 2000. Feedback interactions between cell-cell adherens junctions and cytoskeletal dynamics in newt lung epithelial cells. *Mol. Biol. Cell.* 11:2471–2483.

Waterman-Storer, C. M., J. W. Sanger, and J. M. Sanger. 1993. Dynamics of organelles in the mitotic spindle of living cells: membrane and microtubule interactions. *Cell Motil. Cytoskeleton.* 26:19–39.

Yarmola, E. G., T. Somasundaram, T. A. Boring, I. Spector, and M. R. Bubb. 2000. Actin-latrunculin A structure and function—Differential modulation of actin-binding protein function by latrunculin A. *J. Biol. Chem.* 275:28120–28127.